

Lower Limits on Scalar Ultralight Dark Matter from Optical Cavities

Tejas Deshpande, Andra Ionescu, Nicholas Miller, Zhiyuan Wang, Gerald Gabrielse, Andrew A. Geraci, and Tim Kovachy
*Center for Fundamental Physics, Department of Physics and Astronomy,
Northwestern University, Evanston, Illinois 60208, USA*
(Dated: December 31, 2024)

Oscillations of scalar ultralight dark matter (ULDM) at its Compton frequency would couple to fundamental constants to coherently drive the length of nearby Fabry-Perot cavities. Resulting differences in the length of two cavities are searched for in the spectrum of the beat note between lasers traversing the cavities. The new direct ULDM bounds set near 5 kHz and between 20 and 90 kHz are one to two orders of magnitude lower for two model ULDM distributions – a standard galactic halo, and a relaxation star bound to Earth. Laser filtering and mechanical isolation are critical.

Astronomical and cosmological evidence suggests that 85% of the matter in the Universe is dark matter [1]. It remains to be discovered whether the unidentified dark matter is described by the Standard Model (SM), or requires physics beyond the SM [2]. Familiar axions [3] and WIMPs [4] (weakly interacting massive particles) are proposed dark matter candidates that would also solve the so-called “strong-CP” [5] and “hierarchy” problems [6].

This Letter reports new bounds on a well-motivated alternative – scalar, parity-even, ultralight dark matter (ULDM) that behaves as a classical wave [7]. A broadband search with the apparatus of Fig. 1 is for differing length changes of two cavities at the ULDM Compton frequency $f_\phi \equiv m_\phi c^2 / (2\pi\hbar)$, for ULDM mass m_ϕ , Planck constant \hbar , and speed of light c . Sensitivity to the local dark matter density produces strong and direct limits on boson stars [8, 9] composed of relaxions – a proposed solution to the hierarchy problem [10] – a contrast to the indirect limits from torsion balance equivalence principle (EP) tests [11, 12].

ULDM is well-motivated. It is consistent with the standard halo model (SHM) distribution of dark matter in a galaxy [12], and naturally occurs in BSM (beyond the SM) theories. The topologically complex vacua of string theory, for example, produces many ULDM candidates. These include moduli and dilatons [13–19] that couple to matter by making SM parameters depend on moduli fields. The moduli can acquire mass through supersymmetry (SUSY) breaking at ~ 0.1 meV for TeV scale SUSY [13], or have much lighter masses due to loop factors and small coefficients (e.g. for the electron Yukawa modulus). The electron mass and charge (m_e and $-e$), and the fine structure constant (α), vary in time (t) and space (\mathbf{x}) in proportion to the ULDM field $\phi(t, \mathbf{x})$,

$$\begin{aligned} \frac{\delta\alpha(t, \mathbf{x})}{\alpha} &= d_\alpha \frac{\sqrt{4\pi\hbar c}}{E_P} \phi(t, \mathbf{x}), \\ \frac{\delta m_e(t, \mathbf{x})}{m_e} &= d_{m_e} \frac{\sqrt{4\pi\hbar c}}{E_P} \phi(t, \mathbf{x}). \end{aligned} \quad (1)$$

$E_P \equiv \sqrt{\hbar c^5/G}$ is the Planck energy and G is Newton’s

gravitational constant. The dimensionless coupling constants are d_{m_e} and d_α . The latter is often called d_e [20], but $d_\alpha/2$ is the coupling to electron charge because $\alpha \propto e^2$.

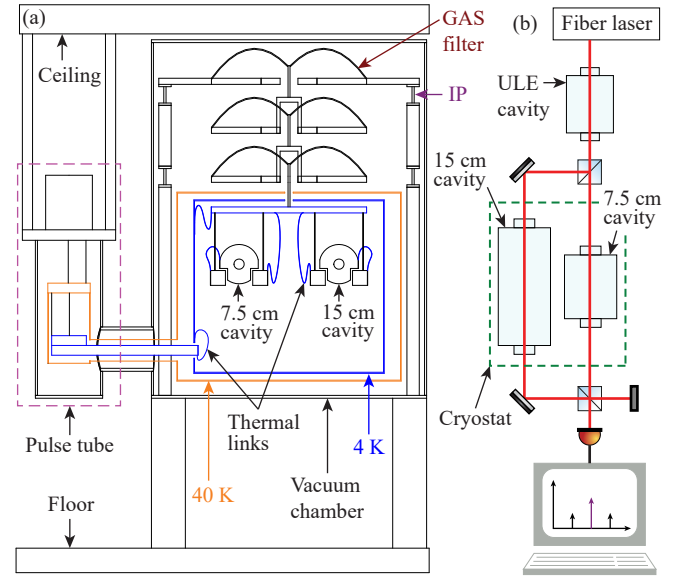


FIG. 1. (a) Side view of the vibrationally-isolated cryostat. (b) Schematic of the optical probe of the differential length variations of two cavities.

The ULDM coherence length, $\lambda_\phi \equiv \hbar / (m_\phi v_{\text{vir}})$ [21] is much larger than our tabletop apparatus for both ULDM models, so $\phi(t, \mathbf{x}) \approx \phi(t)$ in Eq. (1). The virial velocity v_{vir} is for ULDM in equilibrium, with mean kinetic energy equal to $(-1/2)$ multiplied by the mean gravitational potential energy. For the SHM, $v_{\text{vir}} \approx 166$ km/s ([4] and Appendix D) so λ_ϕ ranges from 8×10^2 to 172×10^2 km for the f_ϕ between 5 and 100 kHz on which we set new bounds. For a relaxation star gravitationally bound to the Earth, $v_{\text{vir}} \approx 32$ m/s $\times (f_\phi/1 \text{ kHz})$ [10] so λ_ϕ ranges from 5×10^4 to 110×10^4 km for the 20 to 90 kHz frequency range we consider.

Couplings to ULDM change α and m_e , and hence the

size of atoms and chemical bonds that go as the Bohr radius, $a_B \equiv \hbar/(cm_e \alpha)$. The effective ULDM “strain” driving the length $L_{\text{cav}}(t)$ of a rigid optical cavity is the fractional change in a_B [22, 23]

$$h_{\text{DM}}(t) = -\frac{\delta m_e(t)}{m_e} - \frac{\delta \alpha(t)}{\alpha}. \quad (2)$$

The resulting cavity strain, $h(t) = \delta L_{\text{cav}}(t)/L_{\text{cav}}$, will oscillate at f_ϕ for a continuous drive $h_{\text{DM}}(t)$. Until a nonzero $h_{\text{DM}}(t)$ is detected, limits on $\delta m_e(t)/m_e$ and $\delta \alpha(t)/\alpha$ are set in the usual way [12], by assuming that $\delta \alpha(t)/\alpha = 0$ to place bounds on $\delta m_e(t)/m_e$ and vice versa. The former is reported. It applies for the latter.

The ULDM coherence times $\tau_c \equiv \hbar/(m_\phi v_{\text{vir}}^2)$ [21, 24] can range from short ($\tau_c \ll T_m$) to long ($\tau_c \gg T_m$) compared to our measurement time, $T_m \approx 4 \text{ days} \approx 4 \times 10^5 \text{ s}$. For the relaxation model, the coherence times for the range of f_ϕ we consider go from short ($\tau_c = 2 \times 10^4 \text{ s}$) to long ($\tau_c = 2 \times 10^6 \text{ s}$). For the SHM, the coherence time is always short since τ_c ranges only from 5 s to 10^2 s over the range of f_ϕ we consider.

For long coherence times, $\phi(t) \approx \Phi_0 \cos(2\pi f_\phi t + \theta)$ with a stochastic phase θ , and amplitude $\Phi_0 \sim \sqrt{\rho_{\text{DM}}}$, that goes as the square root of the local dark matter density. For short coherence times, a sum over many Fourier components is required, in a frequency window around f_ϕ with a width that scales as τ_c^{-1} . All components go as $\sqrt{\rho_{\text{DM}}}$. One result is the so-called “ULDM lineshape” [21], an example of which is shown for the SHM in Fig. 2 (a). All coherence times are appropriately accounted for in our Bayesian data analysis ([21, 24] and Appendix D).

Fig. 1 represents the apparatus used to search for ULDM Compton frequencies between 5 and 100 kHz. Fig. 1 (a) is an overview of the passive vibration isolation achieved via 5 stages: an inverted pendulum (IP), three geometric anti-spring (GAS) filters in series, and a 4-wire pendulum. A pulse tube refrigerator maintains the “science cavities” at 6 K. The low temperature will be important for achieving higher sensitivities in the future.

Both of the cryogenic optical cavities are made of single-crystal sapphire due to its high thermal conductivity, large Young’s modulus, and low intrinsic loss at cryogenic temperatures [25]. Their longitudinal axes are parallel to the crystallographic c-axis to maximize longitudinal stiffness. Optically contacted sapphire mirrors are coated with low-Brownian-noise crystalline GaAs/AlGaAs dielectric Bragg reflectors [26].

Fig. 1 (b) is a overview of the cavities and laser system. The amplified light from a fiber laser with frequency $f_{\text{opt}} \approx 193 \text{ THz}$ is Pound-Drever-Hall (PDH) locked [27] to a stable, ultralow expansion (ULE) cavity that is 10 cm long with a finesse of 500,000. The light is then split into beams frequency shifted by $\approx 131 \text{ MHz}$ (Fig. 6) to make them nearly resonant with cavities that are $L_L = 15 \text{ cm}$

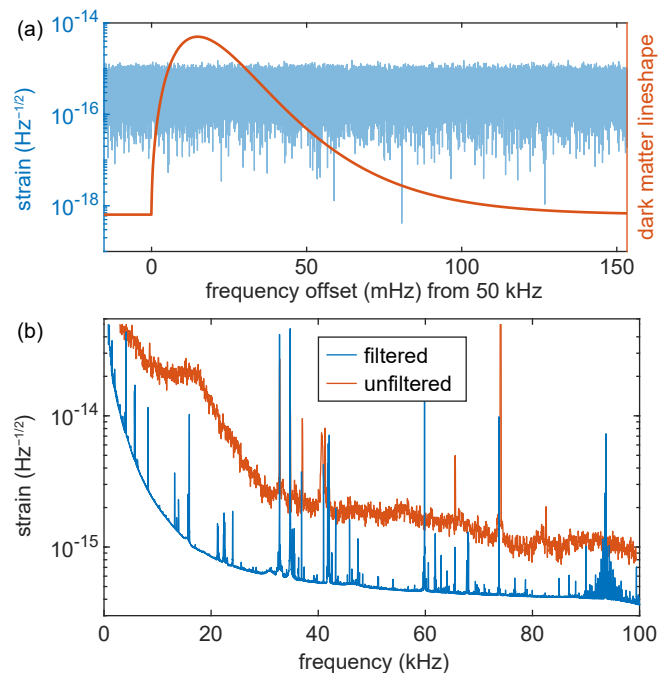


FIG. 2. (a) Orange curve is a normalized analytic curve showing the expected ULDM lineshape in the SHM. Zoom in of the filtered strain ASD in (a) around 50 kHz with $\approx 3 \mu\text{Hz}$ RBW. (b) The averaged ASD of the differential optical strain, $\tilde{h}(f)$, with and without filtering through the ULE cavity.

and $L_S = 7.5 \text{ cm}$ long. The differential “optical strain” for fluctuations $\delta f_{\text{beat}}(t)$ in their 262 MHz beat note is

$$h(t) \equiv \frac{\delta f_{\text{beat}}(t)}{f_{\text{opt}}} = A_{\text{det}}(f_\phi) h_{\text{DM}}(t) + h_{\text{noise}}(t). \quad (3)$$

This cavity response is the “drive” $h_{\text{DM}}(t)$ times a detector response function $A_{\text{det}}(f_\phi)$. The added $h_{\text{noise}}(t)$ from non-ULDM sources is critically reduced, from the orange to blue curves in Fig. 2 (b), by filtering the laser through the ULE cavity. Laser frequency fluctuations offset from a cavity resonance by f are suppressed as $1.5 \text{ kHz}/f$. Contributions to $h_{\text{noise}}(t)$ from vibrations are greatly suppressed by the vibration isolation system.

The ULDM f_ϕ primarily searched for are well above the 4.7 and 7.6 kHz optical poles for the long and short cavities. The detector response function of Eq. (3) then simplifies (Appendix C) to the difference

$$A_{\text{det}}(f_\phi) = |H_{M,L}(f_\phi) - H_{M,S}(f_\phi)|, \quad (4)$$

of two mechanical transfer functions

$$H_M(f_\phi) = (1 + Q_M^{-2})^{1/2} \left(1 - \left(\frac{f_\phi}{f_M} \right)^2 + iQ_M^{-1} \right)^{-1}. \quad (5)$$

Each has its own resonant frequency f_M and large quality factor Q_M . The second subscript in Eq. (4) designates the long (L) or short (S) cavity. Each sapphire cavity acts

on a ULDM signal as a low pass filter, given that Q_M^{-1} is negligible away from f_M . For frequencies above f_M , the cavity does not follow the ULDM-induced oscillations [22].

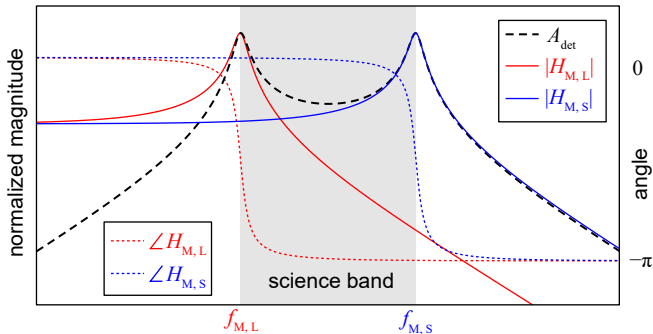


FIG. 3. Qualitative magnitude and phases of two cavities' individual mechanical transfer functions (Eq. (5)), $H_{M,L/S}$ for the long/short cavity, and the detector response function A_{det} (Eq. (4)) with the primary science band highlighted in gray.

Fig. 3 shows magnitudes and phases of low pass transfer functions representing long and short cavities, whose difference determines A_{det} . The highest sensitivity to h_{DM} is in our “science band” between the longitudinal mechanical resonances of the two cavities at $f_{M,L} \approx 34$ kHz and $f_{M,S} \approx 64$ kHz. The short cavity approximately follows the ULDM drive, while the long cavity (largely unaffected by ULDM) is a length reference.

Coherent ULDM sources drive the science cavities identically. A big advantage of the differential detection is that the strains of the two science cavities subtract within the absolute value in Eq. (4), while uncorrelated noise sources $h_{\text{noise}}(t)$ add in quadrature.

The data set for this work is a time series, $h(t)$, of measurements made every $4.63 \mu\text{s}$ for 4 days. Fourier transforming on a 16-core computer for 28 hours produces the amplitude spectral density (ASD) $\tilde{h}(f)$ in Fig. 2 (b). All observed peaks are locally flat in that they are much wider than can be attributed to ULDM. The spectrum is well-described by white Gaussian noise in frequency windows approximately equal to the expected ULDM lineshape's spectral width. The data set is stationary in that the means, variances, and autocorrelation constants are independent of time, implying that neighboring frequency bins of $\tilde{h}(f)$ are uncorrelated. The blue frequency spectrum in Fig. 2 (a) is a raw ULE-cavity-filtered ASD of the differential optical strain, $\tilde{h}(f)$, measured with a resolution bandwidth (RBW) $\approx 3 \mu\text{Hz}$ around $f = 50$ kHz. The orange curve indicates the narrowness of the expected ULDM signal [21] for the SHM. The ASD of the differential optical strain is shown over a larger frequency range in the blue curve in Fig. 2 (b), which is the average of 10^5 spectra with a RBW of ≈ 0.3 Hz. To emphasize the greatly improved sensitivity achieved with ULE cavity filtering, the orange curve in Fig. 2 (b) (for a much smaller

data set with 100 Hz RBW and 25 averages) shows an ASD that is much higher due to unfiltered laser frequency noise.

The ASD of the large data set $\tilde{h}(f)$ is analyzed to look for evidence of the two different ULDM models using Bayesian analysis [21, 24]. In a frequency window as wide as the ULDM lineshape (e.g. Fig. 2 (a)), we compute the likelihood that a ULDM signal \tilde{s}_{DM} (Fourier transform of $A_{\text{det}}h_{\text{DM}}(t)$ for a given d_{m_e}) gives rise to the measured data $\tilde{h}(f)$. We use the likelihood function, $\mathcal{L}(\{\tilde{h}\}|d_{m_e})$, defined in Ref. [21, 24]. The probability distribution function of the unknown parameter d_{m_e} , known as the posterior, $\mathcal{P}(d_{m_e}|\{\tilde{h}\})$, is computed from the likelihood using Bayes theorem (Appendix D). Solving

$$2 \int_0^{d_{m_e}^{95\%}} dd_{m_e} \mathcal{P}(d_{m_e}|\{\tilde{h}\}) = 0.95. \quad (6)$$

gives d_{m_e} at a 95% confidence level.

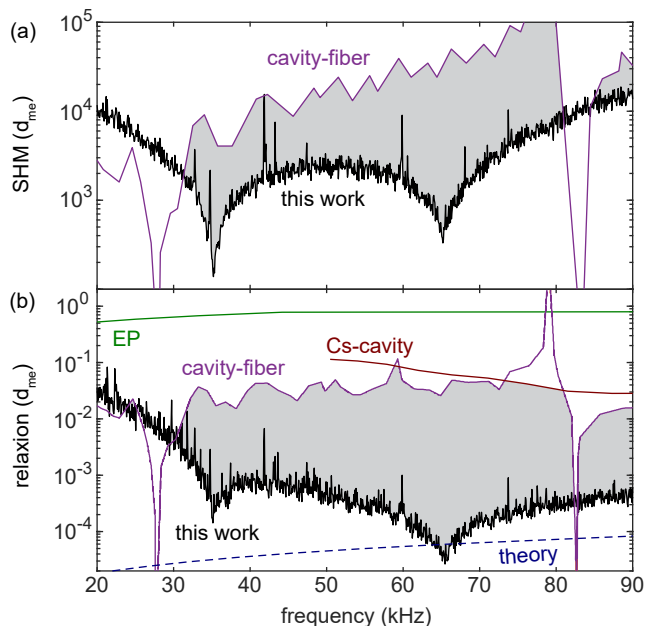


FIG. 4. Bounds on d_{m_e} as a function of ULDM Compton frequency, for the SHM (a) and for a relaxation star bound to Earth (b), with limits from cavity-fiber [28] and Cs-cavity [29] direct ULDM detectors, alongside indirect bounds from equivalence principle (EP) tests [12] and a theoretically motivated target [30].

In Fig. 4 (a), our increased sensitivity (gray area) and much smaller ULDM limits for the SHM (solid black curve) come from solving Eq. (6). This is for a terrestrial detector moving through the galactic dark matter halo towards the Cygnus constellation, as the Solar system orbits the Milky Way, with a relative mean speed of $v_{\text{obs}} \approx 230$ km/s and a Gaussian velocity spread with $v_{\text{vir}} \approx 166$ km/s [4] (Appendix D). We look for spectral peaks in $\tilde{h}(f)$ whose profile and 0.01 to 0.2 Hz widths are

set by the ULDM lineshape and inverse coherence time (Fig. 2 (a)).

In Fig. 4 (b), our increased sensitivity (gray area) and much smaller ULDM limits (solid black curve) for the model of a relaxion star gravitationally bound to Earth are solutions to Eq. (6). The density of this relaxion halo at our detector is a factor of 10^{11} to 10^{13} greater than its SHM counterpart [10], thereby enhancing the limits from our direct ULDM detector by approximately 6 orders of magnitude as compared to the SHM case. For ULDM Compton frequencies less than 34 kHz, for which $\tau_c > T_m$, the d_{me} bound is higher due to the stochastic fluctuation of the ULDM amplitude, Φ_0 , that is included in the Bayesian analysis [24]. In the 64 to 66 kHz range, the bound exceeds a target corresponding to the boundary of the region of parameter space for which Higgs-relaxion mixing can occur [30].

For both models, between 20 to 90 kHz there is no evidence of ULDM above the noise floor of $\tilde{h}(f)$. Peaks visible in Fig. 2 (b) are much broader than expected for a ULDM signal. They likely originate from technical noise sources and thus are part of the noise floor that provides exclusion limits on d_{me} . The previous best limits for both models come from comparing the lengths of a single cavity at different times using an optical fiber delay line (‘cavity-fiber’ curve in Fig. 4) [28].

Fig. 5 displays our SHM result for a much broader range of coupling constants and Compton frequencies to relate the new bounds to other measurement bounds and theoretical constraints. In addition to those shown in Fig. 4 (a) and (b), these include direct ULDM limits from gravitational wave (GW) detectors [31, 32] and the Holometer [33], alongside indirect bounds from EP tests [12, 34, 35]. Radiative corrections to the ULDM mass provide a very model-dependent upper limit on d_{me} , with the parameter space above the dashed line from [12] labeled “naturalness” excluded without substantial fine-tuning [22]. In addition, we set lower limits in the 6 to 10 kHz range for the SHM, where the previous strongest limits came from molecular Iodine spectroscopy [36].

The bounds from this first demonstration of a broadband cavity length comparison method are limited by detector noise that is an order of magnitude above the photon shot noise. Additional laser noise filtering and vibration isolation, along with increased laser power to reduce the shot noise, should make it possible to profit from the cryogenic environment and improve these limits by 3 to 4 orders of magnitude. A longer science cavity and a non-rigid reference cavity [22] would extend the reach to lower ULDM Compton frequencies. The greatly improved broadband sensitivity could be used to search for ULDM from a boson star explosion in a “bosenova” near Earth [9] or from binary black hole and neutron star mergers [37]. Switching from our current broadband methods to resonant methods that use the quality factors of 10^4 already observed could bring very large in-

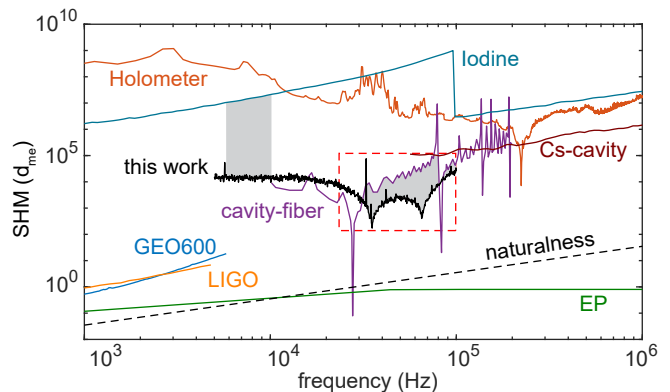


FIG. 5. Bounds on d_{me} for the SHM for a much larger range of d_{me} and Compton frequencies compared to other bounds set by direct and indirect measurements and by theoretical limits. A zoom in of the dashed red box is shown in Fig. 4 (a). See main text for details.

creases in sensitivity. More precise characterization of the mechanical resonance frequencies would allow a much deeper search in future experiments at these particular frequencies (Fig. 7) [38, 39]. Future measurements could even exploit the material properties of cryogenic sapphire cavities to realize quality factor values as high as 10^8 [25, 40].

Two perpendicular cavities would give sensitivity to GWs above the 10 kHz upper limit of LIGO [41]. We estimate a GW strain sensitivity of $\sim 10^{-19} \text{ Hz}^{-1/2}$ at the 34 kHz and 64 kHz mechanical resonances of our current cavities. With the mentioned sensitivity improvements, it could become possible to probe the theoretically well-motivated parameter space for GWs from primordial black hole mergers or gravitationally bound states of QCD axions [41, 42].

In conclusion, a broadband direct ULDM detector sets new lower limits on the coupling of ultralight dark matter (ULDM) and ordinary matter. The new bounds are up to two orders of magnitude lower for both the standard halo model (SHM) and for a relaxion star bound to Earth. Routes to sensitivity increases of 3 to 4 orders of magnitude now seem feasible, with even greater sensitivities at the mechanical resonance frequencies of the optical cavities. Perpendicular cavities could provide gravitational wave sensitivity at frequencies above the 10 kHz limit of current large detectors.

Acknowledgments: The Templeton Foundation funded the apparatus construction and the Packard Foundation funded T. K. B. Odom contributed to early stages of this work, and useful suggestions came from C. Schreiber, A. Derevianko, G. Cole, S. Catano, R. DeSalvo, K. Arai, Y. Michimura, G. Venugopalan, and J. Bourhill. The custom dewar, inverted pendulum, and geometric anti-spring system were built by Four Nine Design to our specifications.

-
- [1] G. Bertone and D. Hooper, *Reviews of Modern Physics* **90**, 045002 (2018).
- [2] M. Safronova, D. Budker, D. DeMille, D. F. J. Kimball, A. Derevianko, and C. W. Clark, *Reviews of Modern Physics* **90**, 025008 (2018).
- [3] C. Adams *et al.*, arXiv preprint arXiv:2203.14923 (2022).
- [4] K. Freese, M. Lisanti, and C. Savage, *Reviews of Modern Physics* **85**, 1561 (2013).
- [5] J. E. Kim and G. Carosi, *Reviews of Modern Physics* **82**, 557 (2010).
- [6] S. Dimopoulos, S. Raby, and F. Wilczek, *Physical Review D* **24**, 1681 (1981).
- [7] E. G. Ferreira, *The Astronomy and Astrophysics Review* **29**, 1 (2021).
- [8] A. Banerjee, G. Perez, M. Safronova, I. Savoray, and A. Shalit, *Journal of High Energy Physics* **2023**, 1 (2023).
- [9] J. Arakawa, J. Eby, M. S. Safronova, V. Takhistov, and M. H. Zaheer, *Physical Review D* **110**, 075007 (2024).
- [10] A. Banerjee, D. Budker, J. Eby, H. Kim, and G. Perez, *Communications Physics* **3**, 1 (2020).
- [11] E. Adelberger, B. Heckel, and A. Nelson, *Annual Review of Nuclear and Particle Science* **53**, 77 (2003).
- [12] D. Antypas *et al.*, arXiv preprint arXiv:2203.14915 (2022).
- [13] S. Dimopoulos and G. F. Giudice, *Physics Letters B* **379**, 105 (1996).
- [14] N. Arkani-Hamed, L. Hall, D. Smith, and N. Weiner, *Physical Review D* **62**, 105002 (2000).
- [15] C. Burgess, A. Maharana, and F. Quevedo, *Journal of High Energy Physics* **2011**, 1 (2011).
- [16] M. Cicoli, C. Burgess, and F. Quevedo, *Journal of High Energy Physics* **2011**, 1 (2011).
- [17] M. Cicoli and F. Quevedo, *Classical and Quantum Gravity* **28**, 204001 (2011).
- [18] T. Taylor and G. Veneziano, *Physics Letters B* **213**, 450 (1988).
- [19] T. Damour and A. M. Polyakov, *Nuclear Physics B* **423**, 532 (1994).
- [20] A. Arvanitaki, J. Huang, and K. Van Tilburg, *Physical Review D* **91**, 015015 (2015).
- [21] A. Derevianko, *Physical Review A* **97**, 042506 (2018).
- [22] A. A. Geraci, C. Bradley, D. Gao, J. Weinstein, and A. Derevianko, *Physical Review Letters* **123**, 031304 (2019).
- [23] H. Grote and Y. V. Stadnik, *Phys. Rev. Res.* **1**, 033187 (2019).
- [24] G. P. Centers, J. W. Blanchard, J. Conrad, N. L. Figueroa, A. Garcon, A. V. Gramolin, D. F. J. Kimball, M. Lawson, B. Pelssers, J. A. Smiga, *et al.*, *Nature Communications* **12**, 7321 (2021).
- [25] X. Korovesi, L. Busch, E. Majorana, P. Puppo, P. Rappagnani, F. Ricci, P. Ruggi, and S. Grohmann, *Physical Review D* **108**, 123009 (2023).
- [26] G. D. Cole, W. Zhang, M. J. Martin, J. Ye, and M. Aspelmeyer, *Nature Photonics* **7**, 644 (2013).
- [27] E. D. Black, *American Journal of Physics* **69**, 79 (2001).
- [28] E. Savalle, A. Hees, F. Frank, E. Cantin, P.-E. Pottie, B. M. Roberts, L. Cros, B. T. McAllister, and P. Wolf, *Physical Review Letters* **126**, 051301 (2021).
- [29] O. Tretiak, X. Zhang, N. L. Figueroa, D. Antypas, A. Brogna, A. Banerjee, G. Perez, and D. Budker, *Physical review letters* **129**, 031301 (2022).
- [30] Y.-D. Tsai, J. Eby, and M. S. Safronova, *Nature Astronomy* **7**, 113 (2023).
- [31] S. M. Vermeulen, P. Relton, H. Grote, V. Raymond, C. Affeldt, F. Bergamin, A. Bisht, M. Brinkmann, K. Danzmann, S. Doravari, *et al.*, *Nature* **600**, 424 (2021).
- [32] A. S. Göttel, A. Ejlli, K. Karan, S. M. Vermeulen, L. Aiello, V. Raymond, and H. Grote, *Physical Review Letters* **133**, 101001 (2024).
- [33] L. Aiello, J. W. Richardson, S. M. Vermeulen, H. Grote, C. Hogan, O. Kwon, and C. Stoughton, *Physical Review Letters* **128**, 121101 (2022).
- [34] S. Schlamminger, K.-Y. Choi, T. A. Wagner, J. H. Gundlach, and E. G. Adelberger, *Phys. Rev. Lett.* **100**, 041101 (2008).
- [35] T. A. Wagner, S. Schlamminger, J. H. Gundlach, and E. G. Adelberger, *Classical and Quantum Gravity* **29**, 184002 (2012).
- [36] R. Oswald, A. Nevsky, V. Vogt, S. Schiller, N. Figueroa, K. Zhang, O. Tretiak, D. Antypas, D. Budker, A. Banerjee, *et al.*, *Physical Review Letters* **129**, 031302 (2022).
- [37] C. Dailey, C. Bradley, D. F. Jackson Kimball, I. A. Sulai, S. Pustelny, A. Wickenbrock, and A. Derevianko, *Nature Astronomy* **5**, 150 (2021).
- [38] A. Arvanitaki, S. Dimopoulos, and K. Van Tilburg, *Phys. Rev. Lett.* **116**, 031102 (2016).
- [39] J. Manley, D. J. Wilson, R. Stump, D. Grin, and S. Singh, *Phys. Rev. Lett.* **124**, 151301 (2020).
- [40] J. Bourhill, E. Ivanov, and M. Tobar, *Physical Review A* **92**, 023817 (2015).
- [41] N. Aggarwal, G. P. Winstone, M. Teo, M. Baryakhtar, S. L. Larson, V. Kalogera, and A. A. Geraci, *Physical Review Letters* **128**, 111101 (2022).
- [42] J. R. Sprague, S. L. Larson, Z. Wang, S. Klomp, A. Laeuger, G. Winstone, N. Aggarwal, A. A. Geraci, and V. Kalogera (LSD Collaboration), *Phys. Rev. D* **110**, 123025 (2024).
- [43] T. Nazarova, F. Riehle, and U. Sterr, *Applied Physics B* **83**, 531 (2006).
- [44] A. Ionescu, PhD thesis, Northwestern University (2025).
- [45] K. Izumi, Cavity response in transmission, Japanese Gravitational Wave Document Database (2012), JGW-T1201121-v2.

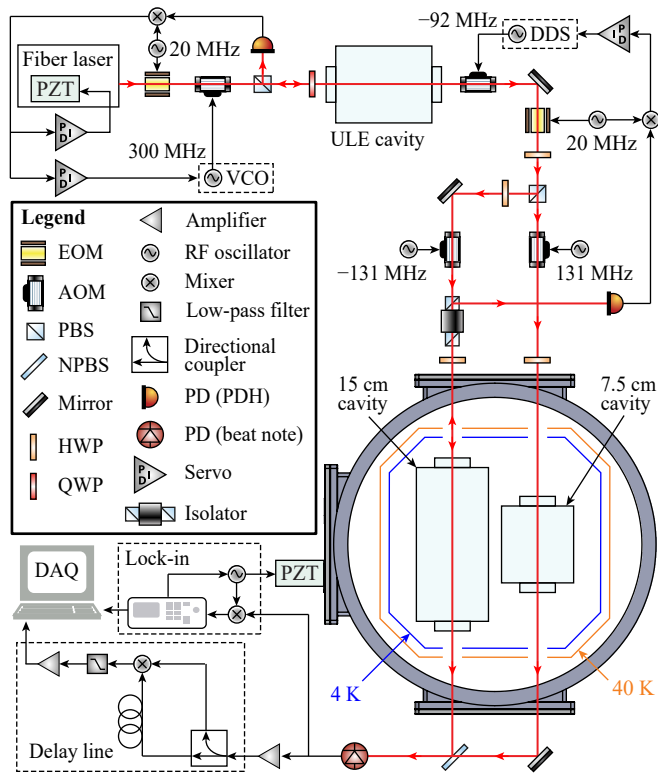


FIG. 6. Detailed optical layout of the cavities' beat note and mechanical resonance measurement apparatus

Appendix A: Isolated Sapphire Cavities at 6 K

Four stages of vibration isolation, each with a mechanical pole ≈ 0.5 Hz, are within the dewar vacuum but operate at 300 K (Fig. 1 (a)). An inverted pendulum (IP), composed of 3 flexures, provides horizontal isolation. The IP supports a stack of 3 geometric anti-spring (GAS) filters that provide vertical isolation after the mass that each supports is tuned within a few grams to produce the mentioned pole frequency. Each GAS is 3 blade springs that meet at a point, from which the stage below is supported.

The fifth stage is a cryogenic 4-wire pendulum with a ≈ 1.5 Hz mechanical pole. The pendulum's Molybdenum wires are $250 \mu\text{m}$ in diameter and 15 cm long. Each of the pendula supports an aluminum plate that, in turn, supports one optical cavity. The optical cavity spacers are supported by the aluminum platforms at 4 points that finite element calculations indicated would minimize vibration transmission [43, 44].

Heat is extracted from the cavities using high conductivity aluminum links that are 0.1 mm by 1 cm by 10 cm long. They are very pure and annealed to maximize the heat transfer, and to make them as flexible as possible to minimize vibration transmission. They are bonded to the sapphire using silver paint and clamped to the cavity platforms. Four-wire silicon diode sensors attached to

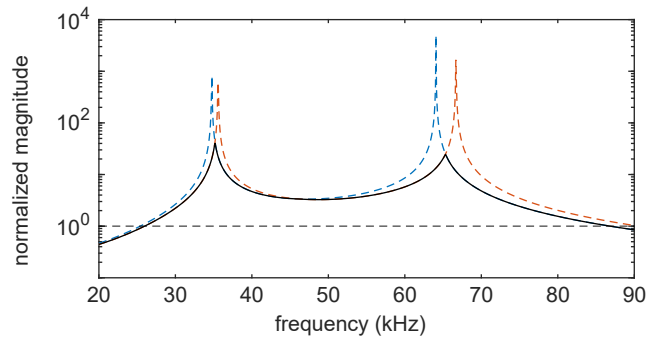


FIG. 7. The blue and orange dashed curves represent A_{det} (Eq. (C1)) for the lowest and highest estimates, respectively, for the longitudinal resonances of the two cavities with the empirically estimated Q_M . The black curve accounts for this uncertainty by conservatively taking the minimum of the two dashed curves.

the cavities with silver paint typically measure 6 K. At this temperature, we estimate a cavity finesse ($\mathcal{F}_{\text{sapph}}$) of $\approx 120,000$.

Appendix B: Optics and Readout of Cavity Length

Fig. 6 gives more optics details for the PDH locking to the ULE cavity, for the frequency shifting to send nearly resonant light through each sapphire cavity, and for slowly compensating the very small frequency drift of these cavities. The fiber laser's internal piezoelectric transducer (PZT) is used for slow feedback (1 kHz) in its PDH lock to the ULE cavity. The fiber amplifier is required because the 40 mW power of the fiber laser was otherwise reduced by the 20 dB attenuation of the narrow band ULE cavity setup, enough to cause the detected signal after the science cavities to be compromised by detector noise. Electro-optic modulators (EOMs) and acousto-optic modulators (AOMs) at the frequencies indicated in the figure are used in usual ways for PDH locking and shifting the laser frequency, along with half- and quarter-wave plates (HWPs and QWPs) and polarizing beam splitters (PBSs) for polarization control. For brevity, the AOMs' double-pass and mode-matching lenses are not shown. The AOMs are driven by analog voltage-controlled oscillators (VCOs) and direct digital synthesizers (DDSs).

The laser beams after the sapphire cavities are recombined on a 50:50 non-polarizing beam splitter (NPBS) and detected with a 5 GHz beat note photodetector (PD, Thorlabs DET08C). The 262 MHz carrier is canceled by mixing with the same output after a delay line. A Fourier transform of the resulting time series from this "self-homodyne detection" is a spectrum as a function of the offset frequency from the carrier, insensitive to slow drifts of the carrier frequency. The discriminator is calibrated

using the signal amplitude when an optical sideband is added with one of the AOMs.

Appendix C: Detector response

A more general detector response function,

$$A_{\text{det}} = |H_{\text{M,L}}H_{\text{OM,L}} - H_{\text{M,S}}H_{\text{OM,S}}|. \quad (\text{C1})$$

is used in our numerical analysis rather than Eq. (4). The optomechanical transfer function is

$$H_{\text{OM}}(f_\phi) = -\frac{if_\phi}{if_\phi + f_p}, \quad (\text{C2})$$

for a cavity pole frequency f_p [44, 45]. In our science band, $f_\phi \gg f_p$ so that $H_{\text{OM}} \approx 1$, making Eq. (4) a good approximation that is useful for an intuitive understanding.

There is uncertainty in our determination of the optical pole frequencies, and also of the mechanical resonance frequencies and quality factors of the two science cavities. The optical poles are estimated using $f_{\text{p,L/S}} = c/(4L_{\text{L/S}}\mathcal{F}_{\text{sapph}})$. The mechanical resonances at $f_{\text{M,L}} \approx 34$ kHz and $f_{\text{M,S}} \approx 64$ kHz, are determined using a combination of finite element analysis and empirical verification by observing enhancement of peaks in the ASD resulting from a PZT drive. The mechanical quality factors are estimated by measuring the full-width at half maximum of the resonance peaks.

The uncertainty in our determination of the optical and mechanical pole frequencies of the two science cavities produces uncertainty in the detector response function. To be conservative, for the full detector response function we use the solid black curve in Fig. 7 in our analysis. This is the minimum of the two most extreme detector response functions (blue and orange dashed curves) we can make using the pole frequencies, resonance frequencies and quality factor values just described. In the future, improved characterization and optimization of the mechanical resonances would permit an improved search near the cavity resonance frequencies.

Appendix D: Data Acquisition and Processing

The DAQ card rated to 216 kS/s recorded $N = 7.48 \times 10^{10}$ samples with 5 significant figures at a sampling in-

terval $\Delta t = 4.63 \mu\text{s}$. The ASD, $\tilde{h}(f_p)$, is a function of the discrete frequency $f_p \equiv p/(N\Delta t)$ for $p \in \llbracket 0, N/2 \rrbracket$.

For $N\Delta t \gg \tau_c$ the power spectral density of the optical strain (i.e. our signal) is

$$\tilde{S}_p = d_{m_e}^2 A_{\text{det}}^2 \langle |\tilde{\phi}_p|^2 \rangle. \quad (\text{D1})$$

where $\tilde{\phi}_p$ is the discrete Fourier transform of the ULDM field and $\langle \dots \rangle$ denote a statistical average. Note that all of the above quantities are implicit functions of the ULDM Compton frequency f_ϕ . Moreover, $\langle |\tilde{\phi}_p|^2 \rangle$ is defined in terms of the ULDM lineshape function F_p as [21]

$$\langle |\tilde{\phi}_p|^2 \rangle \equiv \frac{\pi N}{\Delta t} \Phi_0^2 F_p, \quad (\text{D2})$$

where $\Phi_0 \equiv c\sqrt{2\rho_{\text{DM}}}/(2\pi f_\phi)$. Assuming a 3D velocity distribution of the ULDM to be $f_{\text{DM}}(\mathbf{v}) = (2\pi v_{\text{vir}}^2)^{-3/2} \exp(-(\mathbf{v} - \mathbf{v}_{\text{obs}})^2/(2v_{\text{vir}}^2))$, and ignoring annual modulation, we get

$$F_p \equiv \frac{\tau_c}{\sqrt{2\pi}\eta} e^{-\eta^2 - 2\pi(f_p - f'_\phi)\tau_c} \times \sinh\left(\eta\sqrt{\eta^2 + 4\pi(f_p - f'_\phi)\tau_c}\right), \quad (\text{D3})$$

where $\tau_c \equiv \hbar/(m_\phi v_{\text{vir}}^2)$ is the coherence time, $f'_\phi = f_\phi + m_\phi v_{\text{obs}}^2/(4\pi\hbar)$, and $\eta \equiv v_{\text{obs}}/v_{\text{vir}}$ ($v_{\text{obs}} \equiv |\mathbf{v}_{\text{obs}}|$). For the SHM ($v_{\text{obs}} \approx 230$ km/s and $v_{\text{vir}} \approx 166$ km/s), $\eta \approx 1$ [4]. For the relaxation star bound to Earth (i.e. $v_{\text{obs}} \approx 0$), $\eta \approx 0$. For the latter, ρ_{DM} and v_{vir} become dependent on f_ϕ [10].

Because f_ϕ is a large number of ULDM linewidths ($\sim \tau_c^{-1}$) away from zero ($p = 0$) and from the Nyquist ($p = N/2$) frequency, we can evaluate the likelihood function [21]

$$\mathcal{L}(\{\tilde{d}_p\}|d_{m_e}) \equiv \prod_{p=1}^{N/2-1} \frac{1}{\pi\tilde{\Sigma}_p} \exp\left[-\frac{|\tilde{d}_p|^2}{\tilde{\Sigma}_p}\right], \quad (\text{D4})$$

where $\tilde{d}_p \equiv (N/\Delta t)^{1/2} \tilde{h}(f_p)$ and $\tilde{\Sigma}_p \equiv \tilde{\rho}_p + \tilde{S}_p$. The detector's noise model $\tilde{\rho}_p$ is the averaged $|\tilde{d}_p|^2$.

The posterior can be computed from Eq. (D4) using Bayes theorem

$$\mathcal{P}(d_{m_e}|\{\tilde{d}_p\}) = \frac{p(d_{m_e})}{p(\{\tilde{d}_p\})} \mathcal{L}(\{\tilde{d}_p\}|d_{m_e}). \quad (\text{D5})$$

We assume an uninformed prior, $p(d_{m_e})$, and $p(\{\tilde{d}_p\})$ is a normalization constant. For $N\Delta t \gg \tau_c$, in an approximate analytic solution to Eq. (6), we expect the scaling $d_{m_e} \propto \hbar/(N\Delta t \tau_c)^{1/4}$.